

ModMax Black Holes in 4-Dimensional Einstein-Gauss-Bonnet Gravity

Bilel. Hamil ^{*}

Laboratoire de Physique Mathématique et Subatomique,
Faculté des Sciences Exactes, Université Constantine 1, Constantine, Algeria.

January 7, 2026

Abstract

In this paper, we study charged black hole solutions in 4-dimensional Einstein-Gauss-Bonnet gravity combined with ModMax nonlinear electrodynamics. This is a conformally invariant extension of Maxwell theory that effectively describes nonlinear electromagnetic phenomena. Within the regularized 4-dimensional Gauss-Bonnet framework, we derive an exact static and spherically symmetric black hole solution that is sourced by a purely electric ModMax field. We explore how higher curvature corrections and nonlinear electromagnetic effects change the spacetime geometry, horizon structure, and energy content of the black hole. We examine the thermodynamic properties in detail, revealing a minimum mass and stable black hole remnants. These findings might be significant in scenarios involving dark-sector compact objects or evaporation endpoints beyond standard general relativity. We also investigate the motion of massive particles, discussing the characteristics of circular orbits and the innermost stable circular orbit, highlighting differences from the Maxwell case. Additionally, we analyze the quasinormal modes of a massive scalar field using WKB methods with Padé approximants and the Pöschl-Teller approximation. We explore how the quasinormal spectrum depends on the Gauss-Bonnet coupling, the ModMax parameter, and the scalar field mass. Our results confirm the linear stability of the black hole and offer potential observational signatures of dark-sector inspired modifications of gravity and electrodynamics.

1 Introduction

To address fundamental limitations of general relativity, including spacetime singularities and its incompatibility with quantum theory, and to confront observational challenges such as dark matter and dark energy, numerous modified theories of gravity have been proposed. Such modifications are suggested to be necessary across a wide range of distance scales [1, 2]. The advent of gravitational-wave astronomy provides a unique opportunity to perform stringent tests of these theories in the strong-field regime and to discriminate among competing models [3–6]. Consequently, the study of compact objects within alternative gravitational frameworks, together with their associated observational signatures, plays a crucial role in probing the fundamental laws of gravity.

Among the most extensively studied extensions of General Relativity is Lovelock gravity [7], which generalizes the Einstein-Hilbert action through the inclusion of higher-order curvature invariants. The simplest realization of a second-order Lovelock theory is the Gauss-Bonnet (GB) theory. A key property of Lovelock theories is that their equations of motion remain second order in derivatives, despite the presence of higher-curvature terms. The stability of black hole solutions in these frameworks has been investigated under scalar, vector, and tensor perturbations [8–12], revealing scalar-mode instabilities in five dimensions and tensor-mode instabilities in six dimensions, while no instabilities are observed in other dimensional settings. In the context of string theory, higher-order curvature corrections are known to introduce higher-derivative terms in the metric [13–15], which typically lead to perturbative ghost

^{*}hamilbilel@gmail.com

modes. By contrast, the second-order Lovelock theory in the form of the GB combination [16] does not introduce higher derivatives in the effective string action and is therefore expected to be free of ghost degrees of freedom at this order.

It is well established that general relativity admits static and spherically symmetric black hole solutions in a wide variety of spacetime settings. In 4-dimensions, however, the GB correction to the Einstein-Hilbert action reduces to a topological invariant and therefore does not contribute to the gravitational field equations, thus excluding the existence of black hole solutions distinct from those of general relativity. This makes astrophysical tests of GB gravity in our four-dimensional universe exceptionally challenging. To avoid the requirements of Lovelock's theory and directly introduce the GB term into 4D gravity, Glavan and Lin [17] proposed a 4-dimensional Einstein-Gauss-Bonnet (4D-EGB) theory by rescaling the GB coupling parameter as $\alpha \rightarrow \frac{\alpha}{D-4}$ and subsequently taking the limit $D \rightarrow 4$. A similar regularization procedure was previously proposed by Tomozawa in the context of quantum corrections to Einstein gravity, which led to static and spherically symmetric black hole solutions [18]. This method was subsequently reformulated in a simplified classical Lagrangian framework by Cognola et al. [19], effectively reproducing quantum corrections associated with the GB invariant. Notably, the resulting static and spherically symmetric black hole solutions in 4D-EGB gravity are equivalent to those obtained from semiclassical Einstein equations with conformal anomaly [20], regularized Lovelock gravity [7], and Horndeski scalar-tensor theory [21]. The 4D-EGB theory has since been widely examined in the literature, with numerous studies investigating its black hole solutions, thermodynamic properties, and cosmological implications [22–38]. Nonlinear electrodynamics (NED) was originally developed as a generalization of Maxwell's classical theory in order to address some limitations of Maxwell's theory, particularly the divergence of the electromagnetic field at a point charge. It is well known that, in the regime of strong electromagnetic fields, Maxwell's electrodynamics effectively acquires nonlinear corrections arising from quantum effects [39–41]. In this context, NED has attracted considerable attention in gravitational and cosmological studies. In particular, it has been suggested that the coupling of certain NED models to general relativity may provide a mechanism for cosmic inflation [42]. Moreover, NED frameworks have been shown to play a significant role in addressing spacetime singularities, including those associated with black holes [43, 44]. The Born-Infeld (BI) theory is among the most widely studied NED models. Originally introduced to eliminate the divergence of the self-energy of point-like charges, BI electrodynamics achieves this by imposing an upper bound on the electromagnetic field strength, leading to finite self-energy configurations [45]. Furthermore, BI theory naturally emerges as the effective action describing D-branes and open superstrings. Despite these appealing features, BI electrodynamics does not preserve all the symmetries of Maxwell's theory. Although it exhibits an $SO(2)$ electric–magnetic duality, the presence of a dimensionful parameter prevents it from being conformally invariant [46]. Recently, the Modified Maxwell (ModMax) theory was proposed as a novel NED model that preserves both conformal invariance and electric–magnetic duality by introducing a dimensionless nonlinearity parameter, denoted by γ [47–50]. In the limit $\gamma = 0$, the ModMax theory reduces to standard Maxwell electrodynamics. When coupled to general relativity, ModMax electrodynamics leads to black hole solutions characterized by a tunable nonlinear parameter that effectively screens the electromagnetic charge. The corresponding black hole solution was first obtained in [47, 48], and since then, several of its physical properties have been extensively investigated [51–61].

Even though EGB gravity and the ModMax field have been studied separately, their combined effect on black holes remains largely unexplored. In this work, we study how their interplay influences black hole thermodynamics, stability, and observable properties. We construct a black hole solution with a ModMax field in EGB gravity and analyze its physical behavior. Our results reveal modifications to the horizon structure, thermodynamic phase transitions, and the spectrum of scalar quasinormal modes. These effects lead to distinctive signatures that may be probed observationally. This paper is organized as follows. In Sec.2 we present the black hole solution. The thermodynamic properties are discussed in Sec.3. Geodesic motion is examined in Sec.4, while Sec.5 is devoted to the analysis of quasinormal modes. Finally, our conclusions are summarized in Sec.6.

2 ModMax Black Holes in 4D EGB Gravity

We consider the EGB theory in D dimensions coupled to the ModMax electromagnetic field, described by the action

$$S = \frac{1}{16\pi} \int d^D x \sqrt{-g} [R + \alpha \mathcal{L}^{\text{GB}} - 4\mathcal{L}^{\text{MM}}], \quad (1)$$

where g is the determinant of the metric tensor, R denotes the Ricci scalar, and α is the GB coupling constant. The GB Lagrangian is given by [62]

$$\mathcal{L}^{\text{GB}} = R^2 - 4R_{ab}R^{ab} + R_{abcd}R^{abcd}. \quad (2)$$

In the action (1), \mathcal{L}^{MM} represents the ModMax Lagrangian, which is defined as [47, 48]

$$\mathcal{L}^{\text{MM}} = \mathcal{S} \cosh \gamma - \sqrt{\mathcal{S}^2 + \mathcal{P}^2} \sinh \gamma, \quad (3)$$

where γ is a non-negative dimensionless parameter ($\gamma \geq 0$) ensuring causality and unitarity. The quantities

$$\mathcal{S} = \frac{F_{\mu\nu}F^{\mu\nu}}{4} \quad \text{and} \quad \mathcal{P} = \frac{F_{\mu\nu}\tilde{F}^{\mu\nu}}{4}, \quad (4)$$

are the electromagnetic scalar and pseudoscalar invariants constructed from the Maxwell tensor

$$F_{\mu\nu} = \partial_\mu A_\nu - \partial_\nu A_\mu, \quad (5)$$

and its dual

$$\tilde{F}_{\mu\nu} = \frac{1}{2}\epsilon_{\mu\nu\lambda\rho}F^{\lambda\rho}. \quad (6)$$

It is worth mentioning that the ModMax Lagrangian reduces to the Maxwell theory when $\gamma = 0$. Since we focus on electrically charged black hole solutions, we restrict our analysis to the purely electric case by setting $\mathcal{P} = 0$. By varying the action with respect to the metric $g_{\mu\nu}$ and the gauge potential A_μ , the field equations are obtained as

$$R_{ab} - \frac{1}{2}g_{ab}R + \alpha H_{ab} = 8\pi T_{ab}^{\text{(MM)}}, \quad (7)$$

$$\partial_\mu (\sqrt{-g}\tilde{E}^{\mu\nu}) = 0, \quad (8)$$

where

$$\tilde{E}_{\mu\nu} = \frac{\partial \mathcal{L}^{\text{MM}}}{\partial F^{\mu\nu}} = 2\frac{\partial \mathcal{L}^{\text{MM}}}{\partial \mathcal{S}}F_{\mu\nu}. \quad (9)$$

For a purely electric configuration ($\mathcal{P} = 0$), the conservation Eq. (8) takes the form

$$\partial_\mu (\sqrt{-g}e^{-\gamma}F^{\mu\nu}) = 0. \quad (10)$$

On the other hand, the Lanczos term $H_{\mu\nu}^{\text{(GB)}}$ is given by [62],

$$H_{ab} = 2 \left(RR_{ab} - R_{acd\lambda}R_b^{d\lambda c} - 2R_{adbc}R^{dc} - 2R_{ac}R_b^c \right) - \frac{1}{2}\mathcal{L}^{\text{GB}}g_{ab}. \quad (11)$$

The energy-momentum tensor of the ModMax field is expressed as

$$T^{\text{(MM)}\mu\nu} = 2F^{\mu\sigma}F_\sigma^\nu e^{-\gamma} - 2\mathcal{S}e^{-\gamma}g^{\mu\nu}. \quad (12)$$

We adopt a static, spherically symmetric spacetime in D -dimensional with the metric

$$ds^2 = -\mathcal{F}(r)dt^2 + \frac{1}{\mathcal{F}(r)}dr^2 + r^2d\Omega_{D-2}^2, \quad (13)$$

where

$$d\Omega_{D-2}^2 = d\theta_{D-3}^2 + \sin\theta_{D-3}^2(d\theta_{D-4}^2 + \sin\theta_{D-4}^2(\dots + \sin\theta_2^2(d\theta_1^2 + \sin\theta_1^2d\varphi))), \quad (14)$$

denotes the line element of the $(D-2)$ -dimensional unit sphere.

To describe the electromagnetic field, we assume a purely radial electric field and choose the gauge potential as

$$A_\mu = \varepsilon(r)\delta_\mu^t. \quad (15)$$

Substituting this ansatz into the field equations leads to the differential equation

$$\frac{d}{dr}\left(r^{D-2}\frac{d}{dr}\varepsilon(r)\right) = 0, \quad (16)$$

whose solution is

$$\varepsilon(r) = -\frac{(D-3)q}{r^{D-3}}, \quad (17)$$

where q is an integration constant corresponding to the electric charge.

In four dimensions, the GB term does not contribute dynamically since it is topological. However, following recent developments, this limitation can be overcome by rescaling the coupling constant as [17],

$$\alpha \rightarrow \frac{\alpha}{D-4}, \quad (18)$$

and then taking the limit $D \rightarrow 4$, which yields nontrivial black hole solutions.

Applying the field equations and taking the 4-dimensional limit, we obtain

$$\frac{\mathcal{G}(r)'}{r} + \frac{\mathcal{G}(r)}{r^2} - \alpha \left[\frac{2\mathcal{G}(r)\mathcal{G}(r)'}{r^3} - \frac{\mathcal{G}(r)^2}{r^4} \right] + \frac{q^2}{r^4}e^{-\gamma} = 0. \quad (19)$$

with

$$\mathcal{F}(r) = 1 + \mathcal{G}(r). \quad (20)$$

The general solution of Eq. (19) is given by

$$\mathcal{G}(r) = \frac{r^2}{2\alpha} \left(1 \pm \sqrt{1 + \frac{4\alpha}{r^2} \left(\frac{2M}{r} - \frac{q^2}{r^2}e^{-\gamma} \right)} \right). \quad (21)$$

Consequently, the metric function for the four-dimensional EGB black hole coupled to the ModMax field becomes

$$\mathcal{F}(r) = 1 + \frac{r^2}{2\alpha} \left(1 \pm \sqrt{1 + \frac{4\alpha}{r^2} \left(\frac{2M}{r} - \frac{q^2}{r^2}e^{-\gamma} \right)} \right). \quad (22)$$

In the limit $\alpha \rightarrow 0$, the solution admits two asymptotic branches,

$$\mathcal{F}(r) = 1 - \frac{2M}{r} + \frac{q^2}{r^2}e^{-\gamma}, \quad (23)$$

and

$$\mathcal{F}(r) = 1 + \frac{r^2}{\alpha} + \frac{2M}{r} - \frac{q^2}{r^2}e^{-\gamma}. \quad (24)$$

The negative branch reduces to the ModMax solution, while the positive branch does not lead to a physically meaningful solution as the positive sign in the mass term indicates instabilities of the graviton [63]. We therefore restrict our analysis to the negative branch.

We analyze the effects of the ModMax parameter γ , and the GB coupling α on the metric function given in Eq. (22). The behavior of $\mathcal{F}(r)$ as a function of r is displayed in Fig. 1. Depending on the values of γ and α , the spacetime may be horizonless, possess a single event horizon r_+ , or admit two distinct positive roots r_\pm corresponding to an inner (Cauchy) horizon r_- and an outer event horizon r_+ , with $r_+ > r_-$.

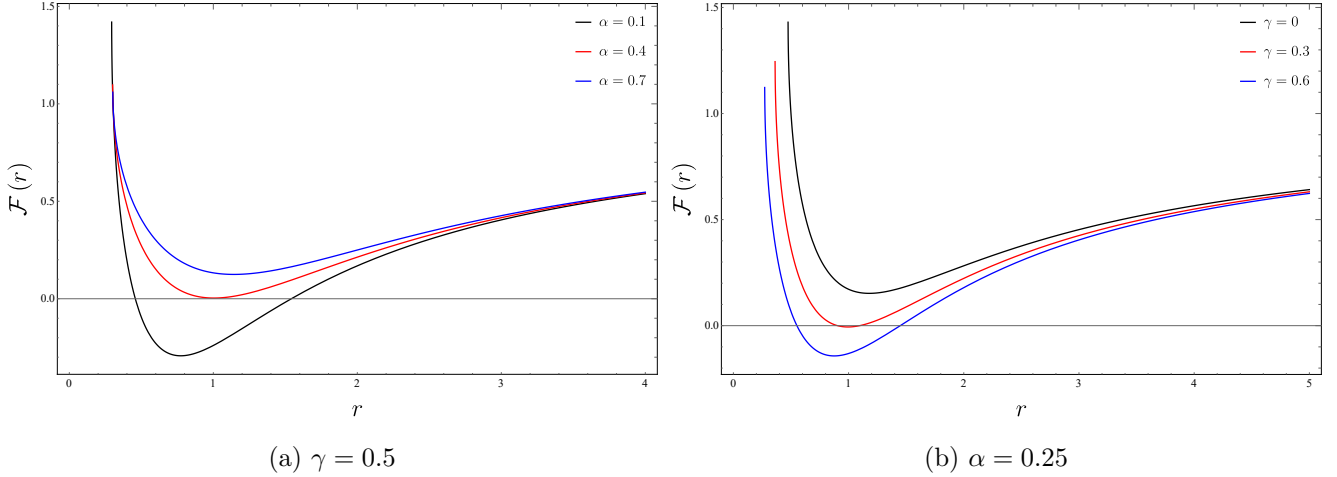


Figure 1: Metric function $\mathcal{F}(r)$ as a function of the radial coordinate r . Parameters: $M = 1$, $q = 1$.

3 Thermodynamics

To investigate the thermodynamic properties of black holes in ModMax–EGB gravity, we first express the black hole mass M in terms of the event horizon radius r_+ , the electric charge q , the ModMax parameter γ , and the GB coupling constant α . This can be achieved by solving the horizon equation $\mathcal{F}(r_+) = 0$, which leads to

$$M = \frac{r_+}{2} \left(1 + \frac{\alpha}{r_+^2} + \frac{q^2}{r_+^2} e^{-\gamma} \right). \quad (25)$$

We now analyze the behavior of the black hole mass in different limits. In the small-horizon limit $r_+ \rightarrow 0$, the black hole goes to

$$\lim_{r_+ \rightarrow 0} M = \frac{q^2 e^{-\gamma} + \alpha}{2r_+}, \quad (26)$$

indicating that the mass depends explicitly on the electric charge, the ModMax parameter, and the GB coupling. In contrast, in the asymptotic limit, $r_+ \rightarrow \infty$, the mass behaves as

$$\lim_{r_+ \rightarrow \infty} M = \frac{r_+}{2}, \quad (27)$$

which shows that the mass becomes independent of α , q and γ .

The behavior of the mass as a function of the horizon radius is illustrated in Fig. 2, for different values of α and γ . The mass exhibits a minimum value $M_{\min} = \sqrt{e^{-\gamma} q^2 + \alpha}$, which occurs at $r_0 = \sqrt{e^{-\gamma} q^2 + \alpha}$. This minimum mass increases with increasing q and α , while it decreases with increasing γ . The existence of a minimum mass suggests that black holes cannot evaporate completely via Hawking radiation, leaving behind a stable remnant with mass M_{\min} . Furthermore, as $r_+ \rightarrow 0$, the black hole mass diverges at the origin.

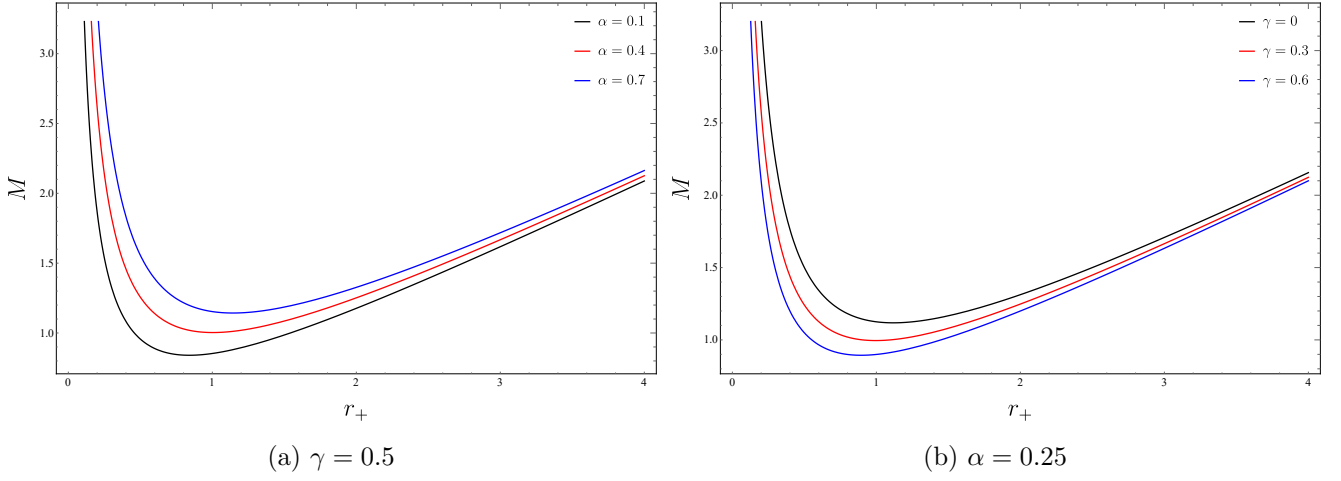


Figure 2: Black hole mass M versus event horizon radius r_+ for $q = 1$.

The Hawking temperature is defined as

$$T = \frac{\kappa}{2\pi}, \quad (28)$$

where κ is the surface gravity defined as $\kappa = \frac{1}{2\pi} \frac{\partial}{\partial r} \mathcal{F}(r) \big|_{r=r_+}$. Using the metric function in (22), the Hawking temperature for these black holes takes the form

$$T = \frac{1}{4\pi r_+} \frac{1 - \frac{\alpha + e^{-\gamma} q^2}{r_+^2}}{1 + \frac{2\alpha}{r_+^2}}. \quad (29)$$

It is clear that the Hawking temperature depends on the GB coupling α , the electric charge q , and the ModMax parameter γ . Notably, small black holes with $r_+ < \sqrt{\alpha + e^{-\gamma} q^2}$, are not physical, as the temperature becomes negative in this region.

Fig. 3 shows the Hawking temperature as a function of r_+ . During evaporation, the temperature increases until it reaches a maximum value T^{\max} at a critical horizon radius r_{crt} , after which it rapidly decreases and vanishes. The existence of a maximum temperature signals a second-order phase transition, at which the specific heat diverges. This maximum temperature increases with γ and decreases with α .

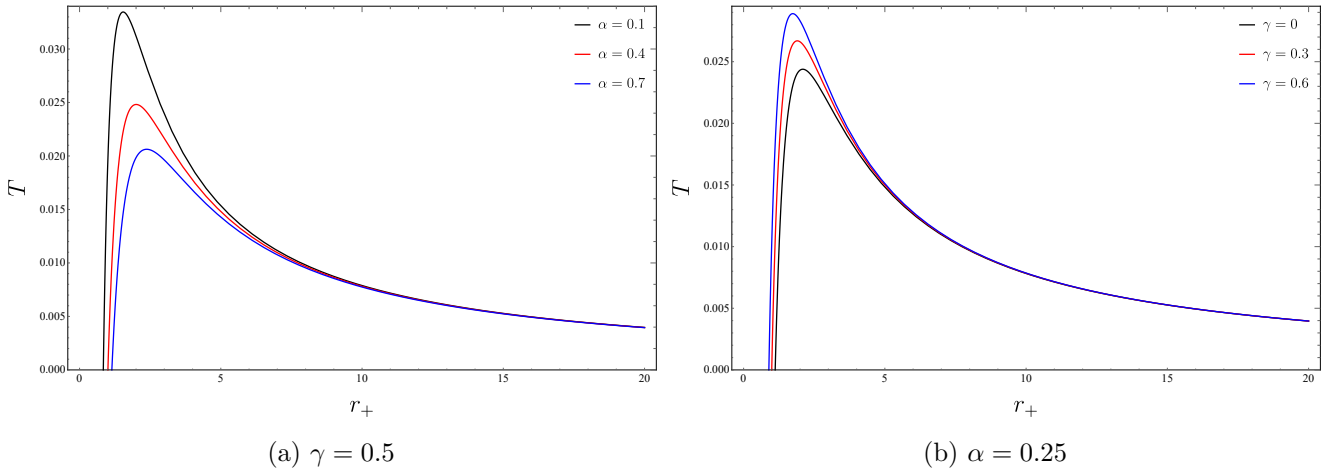


Figure 3: The Hawking temperature as a function of the event horizon r_+ for $M = 1$ and $q = 1$.

We now turn to the black hole entropy. In general, the first law of black hole thermodynamics is

written as

$$dM = TdS + \Phi dq, \quad (30)$$

where $\Phi = \left(\frac{\partial M}{\partial q} \right)_S$ denotes the electric potential. In this work, we restrict our analysis to fixed electric charge, i.e. $dq = 0$, so that the first law reduces to

$$dM = TdS. \quad (31)$$

Consequently, the entropy can be computed from

$$S = \int \frac{dM}{T} = \int \frac{\partial M}{\partial r_+} \frac{dr_+}{T}. \quad (32)$$

Using Eqs. (25), and (29), we obtain the entropy in the form

$$S = \pi r_+^2 + 4\pi\alpha \ln r_+. \quad (33)$$

Interestingly, the ModMax parameter γ does not contribute to the entropy, which depends only on the horizon radius and the GB coupling.

The specific heat provides crucial information about the local thermodynamic stability of the system. A positive specific heat ($C_q > 0$) corresponds to a stable configuration, whereas a negative specific heat ($C_q < 0$) indicates instability. The specific heat at constant charge is defined as

$$C_q = T \left(\frac{\partial S}{\partial T} \right)_q. \quad (34)$$

Employing Eqs. (29) and (33), the specific heat is obtained as

$$C_q = -2\pi r_+^2 \frac{\left(1 - \frac{\alpha + q^2 e^{-\gamma}}{r_+^2}\right) \left(1 + \frac{2\alpha}{r_+^2}\right)^2}{\left(1 - \frac{2\alpha}{r_+^2}\right) \left(1 - \frac{\alpha + e^{-\gamma} q^2}{r_+^2}\right) - 2 \frac{q^2 e^{-\gamma} + \alpha}{r_+^2} \left(1 + \frac{2\alpha}{r_+^2}\right)}. \quad (35)$$

The roots of the heat capacity ($C_q = 0$) define the physical limitation points separating physical ($T > 0$) and non-physical ($T < 0$) black holes. Solving Eq. (29), yields a single positive root,

$$r_{\text{root}} = \sqrt{\alpha + e^{-\gamma} q^2}. \quad (36)$$

The divergence points of the heat capacity correspond to phase transition points and are determined by solving $\frac{\partial T}{\partial r_+} = 0$, which leads to

$$r_1 = \sqrt{\frac{3q^2 e^{-\gamma} + 5\alpha}{2}} - \frac{1}{2} \sqrt{(9q^2 e^{-\gamma} + 11\alpha)(q^2 e^{-\gamma} + 3\alpha)}, \quad (37)$$

$$r_2 = \sqrt{\frac{3q^2 e^{-\gamma} + 5\alpha}{2}} + \frac{1}{2} \sqrt{(9q^2 e^{-\gamma} + 11\alpha)(q^2 e^{-\gamma} + 3\alpha)}. \quad (38)$$

Fig.4 displays the behavior of the specific heat. The analysis reveals two locally stable and physical regions: $0 < r_+ < r_1$ and $r_{\text{root}} < r_+ < r_2$, where both the temperature and the specific heat are positive. In contrast, black holes in the ranges $r_1 < r_+ < r_{\text{root}}$ and $r_+ > r_2$ are thermodynamically unstable or non-physical. Increasing α shifts r_{root} and $r_{1,2}$ to larger values, thereby enlarging the stability regions. Conversely, increasing γ reduces these regions, and in the limit $\gamma \rightarrow \infty$, only one divergence point remains,

$$r_{\text{divergence}} = \sqrt{\frac{5 + \sqrt{33}}{2}} \alpha. \quad (39)$$

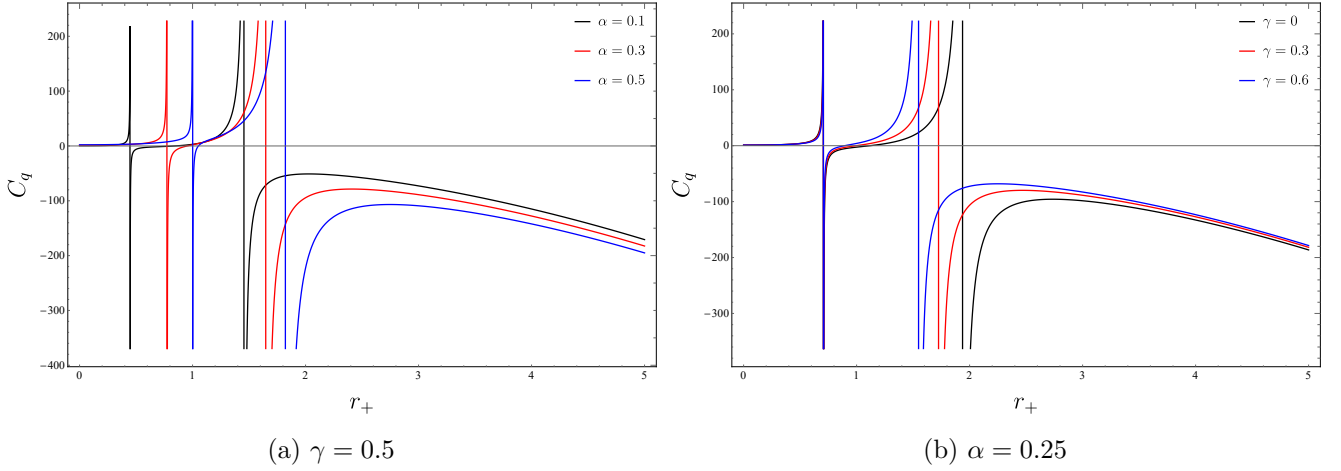


Figure 4: The specific heat as a function of the event horizon r_+ for $M = 1$ and $q = 1$.

Finally, we examine the global thermodynamic stability using the Helmholtz free energy in the canonical ensemble. A negative Helmholtz free energy indicates global stability. The Helmholtz free energy is defined as

$$F = M - TS. \quad (40)$$

Substituting Eqs. (25), (29) and (33), we obtain

$$F = \frac{r_+}{2} \left(1 + \frac{\alpha}{r_+^2} + \frac{q^2}{r_+^2} e^{-\gamma} \right) - \frac{r_+^2 + 4\alpha \ln r_+}{4r_+} \frac{1 - \frac{\alpha + e^{-\gamma} q^2}{r_+^2}}{1 + \frac{2\alpha}{r_+^2}}. \quad (41)$$

Since Eq.(41) cannot be solved analytically, we determine its roots numerically for different values of α , q and γ . The numerical results, presented in Table (1), show that increasing α or q increases the root r_F , thereby enlarging the region of global stability. In contrast, increasing the ModMax parameter γ decreases r_F .

$q = 0.5$ and $\gamma = 0.3$		$q = 0.5$ and $\alpha = 0.25$		$\gamma = 0.3$ and $\alpha = 0.25$	
α	r_F	γ	r_F	q	r_F
0.2	0.200437	0	0.215791	0.1	0.194201
0.4	0.236233	0.2	0.2131	0.2	0.197233
0.6	0.257427	0.4	0.210573	0.3	0.201616
0.8	0.272143	0.6	0.208239	0.4	0.206665
1	0.283146	0.8	0.206117	0.5	0.211814

Table 1: Numerical values of the horizon radius r_F at which the Helmholtz free energy vanishes for different values of the parameter α , γ and q .

Fig.5 displays the Helmholtz free energy as a function of r_+ . The globally stable region corresponds to $r_+ < r_F$, where the free energy is negative. For $r_+ > r_F$ the Helmholtz free energy becomes positive, indicating that large black holes in ModMax–EGB gravity are not globally stable, while small black holes are globally stable configurations.

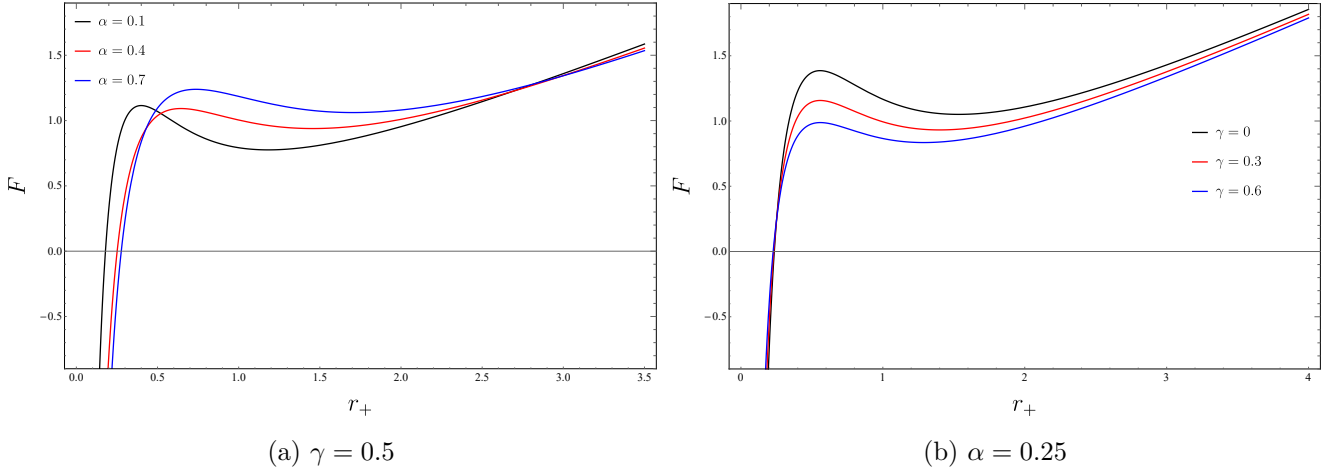


Figure 5: The Helmholtz free energy as a function of the event horizon r_+ for $M = 1$ and $q = 1$.

4 Geodesic motion

We now analyze the dynamics of a test particle moving around an EGB black hole in the presence of a ModMax field. To this end, we write the Lagrangian \mathcal{L} of the test particle associated with the metric (22) as

$$\mathcal{L} = \frac{1}{2} g_{\mu\nu} \dot{x}^\mu \dot{x}^\nu = \frac{1}{2} \left(-\mathcal{F}(r) \dot{t}^2 + \frac{1}{\mathcal{F}(r)} \dot{r}^2 + r^2 \dot{\theta}^2 + r^2 \sin^2 \theta \dot{\varphi}^2 \right), \quad (42)$$

where the dot denotes differentiation with respect to the affine parameter τ .

The spacetime admits two conserved quantities:

$$E = -\frac{\partial \mathcal{L}}{\partial \dot{t}} = \mathcal{F}(r) \dot{t}, \quad L = \frac{\partial \mathcal{L}}{\partial \dot{\varphi}} = r^2 \sin^2 \theta \dot{\varphi}, \quad (43)$$

corresponding to the energy and angular momentum of the particle, respectively.

In addition to these relations, the geodesic equation satisfies

$$-\mathcal{F}(r) \dot{t}^2 + \frac{1}{\mathcal{F}(r)} \dot{r}^2 + r^2 \dot{\theta}^2 + r^2 \sin^2 \theta \dot{\varphi}^2 = -\eta. \quad (44)$$

where $\eta = 0$ for massless particles and $\eta = 1$ for massive particles. Due to the static and spherically symmetric nature of the metric, the motion can be confined to the equatorial plane, i.e., $\theta = \pi/2$. The radial equation of motion then reads

$$\dot{r}^2 + \mathcal{F}(r) \left(\eta + \frac{L^2}{r^2} \right) = E^2. \quad (45)$$

Alternatively, this can be expressed as

$$\dot{r}^2 + V_{\text{eff}}(r) = E^2, \quad (46)$$

with

$$V_{\text{eff}}(r) = \left(\eta + \frac{L^2}{r^2} \right) \mathcal{F}(r). \quad (47)$$

is the effective potential.

4.1 Massive particle

For massive particles in the equatorial plane, the effective potential can be expressed as

$$V_{\text{eff}}(r) = \left(1 + \frac{L^2}{r^2}\right) \mathcal{F}(r). \quad (48)$$

It is important to note that the effective potential for massive particles also vanishes at the horizons. Figure 6 illustrates the behavior of the effective potential for different parameter values. We observe that the GB constant α and the ModMax parameter γ significantly influence the shape of the graph and the nature of observer orbits.

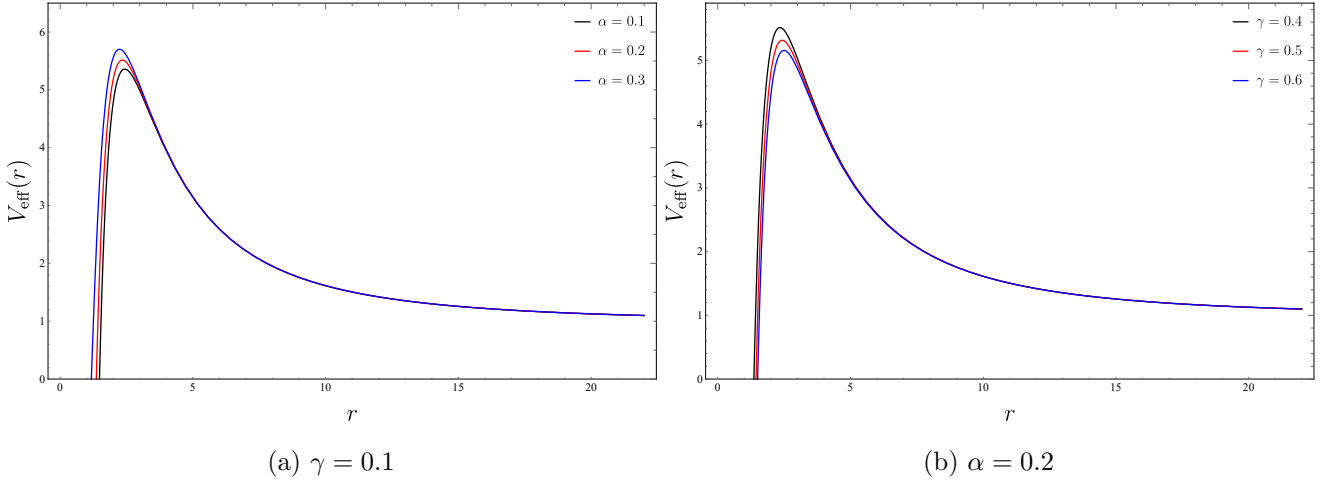


Figure 6: The effective potential as a function of radial distance for $M = 1$, $q = 1$ and $\ell = 10$

Now, let us focus on Eq. (48), which relates the energy and the effective potential, governing the motion of particles. Considering non-radial geodesics with $L = 10$ for a black hole of unit mass $M = 1$, charge $q = 1$, and parameters $\alpha = 0.1$, $\gamma = 0.4$, we analyze the motion of a test particle along non-radial time-like geodesics (see Fig. 7):

- If $E > E_3$, and the particle starts from rest at a finite radius r_0 , it will fall directly into the singularity. This corresponds to a plunge orbit, where the particle begins at r_0 and plunges toward the center.
- If $E = E_3$, the particle can occupy the unstable circular orbit at the maximum of the effective potential. This orbit is marginally unstable: an infinitesimal perturbation causes the particle either to escape outward or plunge into the singularity.
- If $E = E_1$, the motion is bound. If the particle starts from rest at a radius r_1 smaller than that of the stable circular orbit, it initially moves inward, reaches an inner turning point, then reverses direction, oscillating between two finite radii. Conversely, if the particle starts from rest at a radius r_3 larger than that of the stable circular orbit, it initially moves outward, reaches an outer turning point, and then falls back inward. In both cases, the particle undergoes bounded radial motion around the stable circular orbit, neither plunging into the singularity nor escaping to infinity.

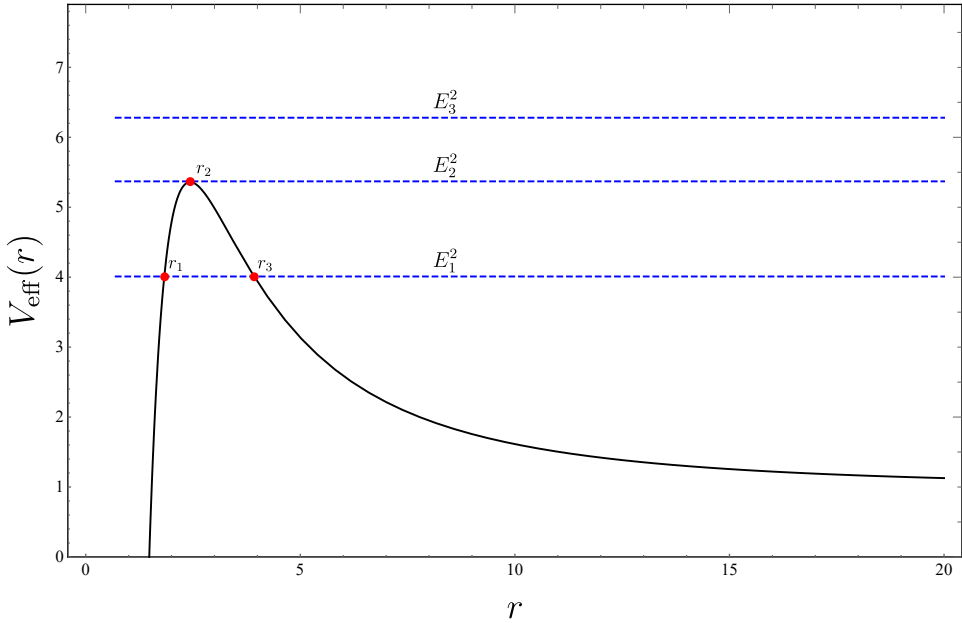
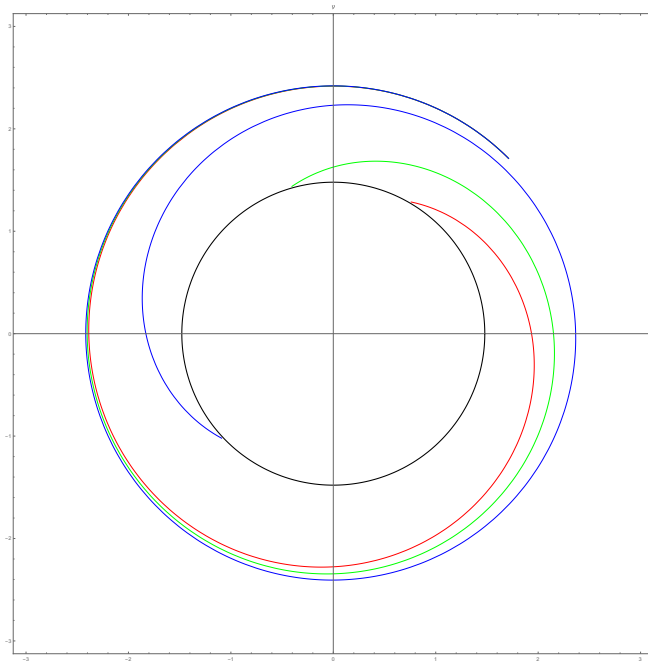
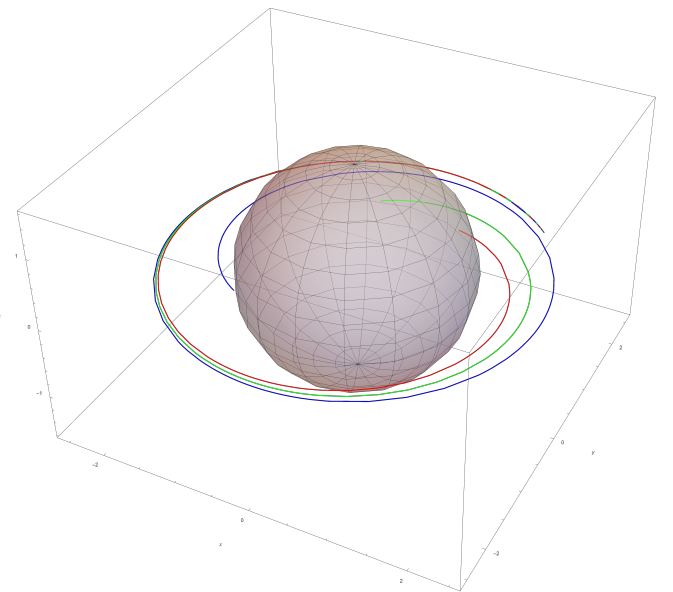


Figure 7: The effective potential of massive particle for $L = 10$, $M = 1$, $q = 1$, $\alpha = 0.1$ and $\gamma = 0.4$

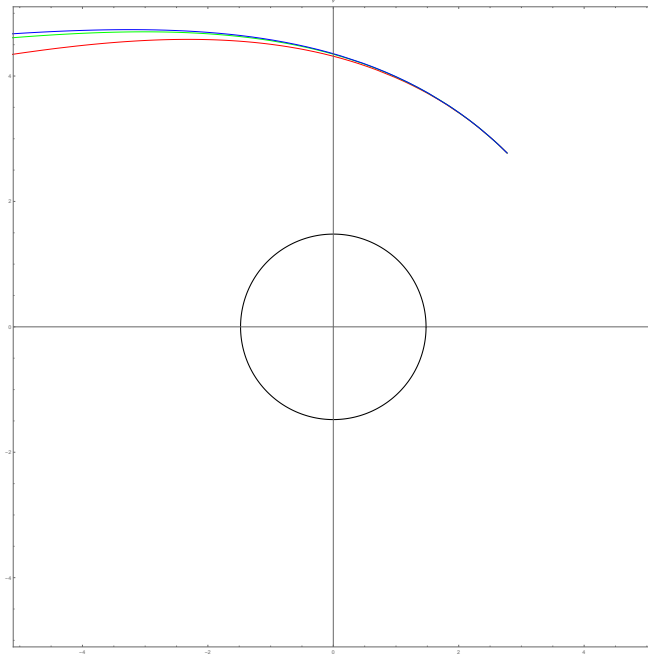
Fig.8 shows massive-particle trajectories for different initial velocities. In panel 8a, the particle is initially placed at $r = r_1$, corresponding to the unstable circular orbit. Small changes in the initial velocity destabilize the orbit, causing the particle to plunge inward and cross the event horizon after a finite time. In contrast, panel 8c depicts a particle released from rest at $r = r_3$, which lies outside the stable circular orbit and has energy lower than that of the unstable orbit. For different initial velocities, the motion remains bounded, and the particle oscillates between two turning points without crossing the horizon.



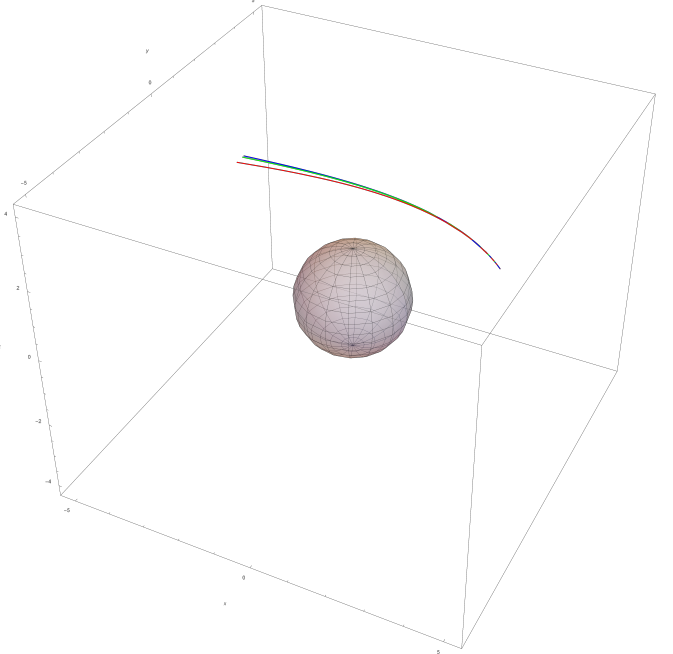
(a) r_2



(b) r_2



(c) r_3



(d) r_3

Figure 8: Trajectories of massive particle for different initial velocities. Parameters: $M = 1$, $q = 1$

Next, we study circular orbits for test particles around a ModMax black hole in EGB gravity. For circular motion, the radial velocity must vanish, $\dot{r} = 0$, and no external radial forces act, $\ddot{r} = 0$. These conditions yield the radial profiles of the specific angular momentum and specific energy of particles in circular orbits confined to the equatorial plane ($\frac{\pi}{2} = 0$), given by

$$L^2 = \frac{r^4}{2\alpha} \frac{1 + \frac{2\alpha m}{r^3} - \sqrt{1 + \frac{8\alpha m}{r^3} - \frac{4\alpha e^{-\gamma} q^2}{r^4}}}{\frac{3m}{r} - \frac{2q^2 e^{-\gamma}}{r^2} - \sqrt{1 + \frac{8\alpha m}{r^3} - \frac{4\alpha e^{-\gamma} q^2}{r^4}}}, \quad (49)$$

$$E^2 = -\frac{r^4}{4\alpha^2} \frac{\sqrt{1 + \frac{8\alpha m}{r^3} - \frac{4\alpha e^{-\gamma} q^2}{r^4}} \left(1 + \frac{2\alpha}{r^2} - \sqrt{1 + \frac{8\alpha m}{r^3} - \frac{4\alpha e^{-\gamma} q^2}{r^4}}\right)^2}{\frac{3m}{r} - \frac{2q^2 e^{-\gamma}}{r^2} - \sqrt{1 + \frac{8\alpha m}{r^3} - \frac{4\alpha e^{-\gamma} q^2}{r^4}}}. \quad (50)$$

The variation of energy with respect to parameters α and γ is shown in Fig. 9. This figure reveals a minimum energy value corresponding to the lowest point on the curve, which decreases as the GB coupling α increases, while it increases with the ModMax parameter γ . Simultaneously, the radius of the inner circular orbit shifts inward.

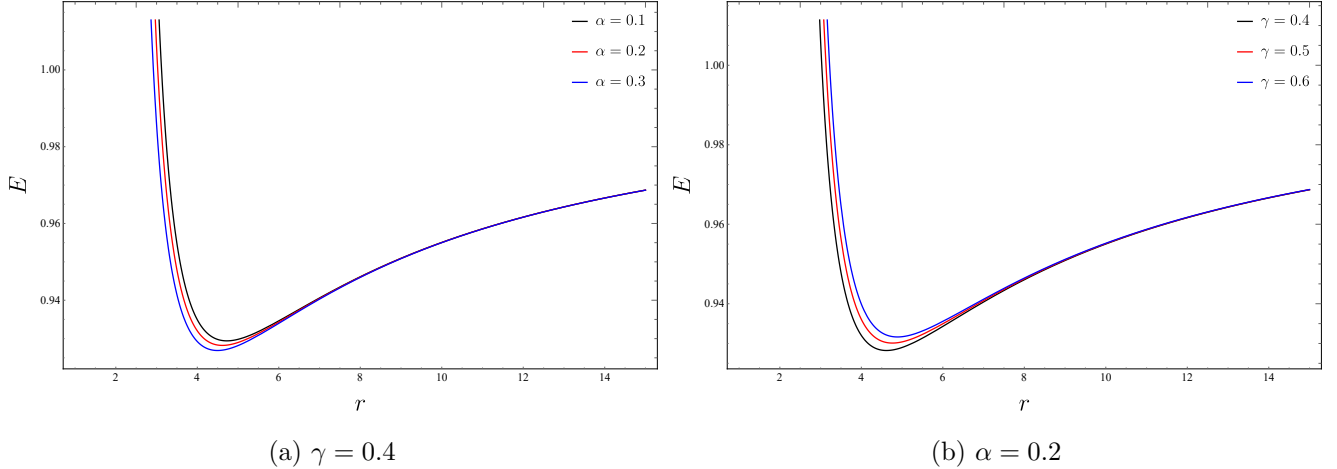


Figure 9: The radial profiles of E of the circular orbits. Parameters: $M = 1$, $q = 1$.

Determining the innermost stable circular orbit (ISCO), where the maximum and minimum of the effective potential coincide, is of critical importance. This requires an additional condition for the ISCO radius, given by the second derivative of the effective potential with respect to r :

$$\frac{d^2}{dr^2} V_{\text{eff}}(r) = 0. \quad (51)$$

By applying this condition together with Eqs.(48) and (49) we obtain

$$r\mathcal{F}(r)''\mathcal{F}(r) + 3\mathcal{F}(r)'\mathcal{F}(r) - 2r\mathcal{F}(r)'^2 = 0. \quad (52)$$

Due to the complexity of this equation, we provide numerical values for the ISCO radius r_{ISCO} , angular momentum L_{ISCO} and energy E_{ISCO} which are tabulated in Table 2 for various cases. As shown in Table 2, the ISCO radius decreases with increasing GB coupling constant α . This indicates that stronger GB effects allow stable orbits closer to the black hole, thereby reducing the ISCO radius. Conversely, an increase in the ModMax parameter γ results in a larger ISCO radius, implying that ModMax nonlinear electrodynamic effects push the innermost stable orbit farther from the black hole.

$\gamma = 0.5$				$\alpha = 0.3$			
α	r_{ISCO}	L_{ISCO}	E_{ISCO}	γ	r_{ISCO}	L_{ISCO}	E_{ISCO}
0.1	4.86399	3.05457	0.928577	0	3.2872	3.3246	0.963621
0.2	4.76186	3.05208	0.928361	0.1	3.7685	3.12838	0.936962
0.3	4.65113	3.05076	0.928242	0.2	4.07486	3.07715	0.930989
0.4	4.52954	3.05122	0.928285	0.3	4.30734	3.05832	0.928988
0.5	4.39372	3.05448	0.928602	0.4	4.49491	3.05175	0.928336
0.6	4.23809	3.06254	0.929423	0.5	4.65113	3.05076	0.928242
0.7	4.05222	3.07977	0.931278	0.6	4.7838	3.05252	0.928399
0.8	3.81147	3.11883	0.935805	0.8	4.89795	3.05564	0.928669

Table 2: Values of the Innermost Stable Circular Orbit radius r_{ISCO} , angular momentum L_{ISCO} and energy E_{ISCO} for a massive particle. Parameters: $M = 1$, $q = 1$.

5 Quasinormal Modes

To explore the quantum aspects of ModMax black holes in EGB gravity, we study their kinematical properties, which offer important indications regarding their semiclassical behavior. Theoretically, black hole perturbations originate from two distinct mechanisms: the introduction of external test fields into the spacetime, or by perturbing the metric itself, i.e., through gravitational perturbations. The most straightforward approach to studying perturbations induced by external fields is to examine the scalar wave equation in the black hole background. For this reason, we focus on the perturbations of a massive scalar field in the vicinity of ModMax black holes in EGB gravity. Therefore, we can express the Klein-Gordon equation in a curved spacetime as follows:

$$\left(\frac{1}{\sqrt{-g}} \partial_\sigma \sqrt{-g} g^{\sigma\rho} \partial_\rho - \mu^2 \right) \phi = 0. \quad (53)$$

where μ is scalar field mass. To solve this equation, we employ a separation of variables Ansatz for the scalar field:

$$\phi(r, \theta, \varphi, t) = \sum_{\ell=0}^{\infty} \sum_{\nu=-\ell}^{\ell} e^{-i\omega t} \frac{u_\ell(r)}{r} \mathcal{Y}_\ell^\nu(\theta, \varphi), \quad (54)$$

where ω are the complex QNM frequencies of scalar perturbations, $\mathcal{Y}_\ell^\nu(\theta, \varphi)$ are the standard spherical harmonics, and $u_\ell(r)$ is the radial wave function. Substituting this Ansatz into Eq.(53) allows us to isolate the radial part of the equation. After manipulation, the radial function $u_\ell(r)$ is found to obey a wave equation of the form:

$$\left[\mathcal{G}(r) \frac{d}{dr} \left(\mathcal{G}(r) \frac{d}{dr} \right) + \omega^2 - \mathcal{U}_{\text{eff}}(r) \right] u_\ell(r) = 0, \quad (55)$$

where the effective potential $\mathcal{U}_{\text{eff}}(r)$ is given by:

$$\mathcal{U}_{\text{eff}}(r) = \mathcal{G}(r) \left(\frac{1}{r} \frac{d}{dr} \mathcal{G}(r) + \frac{\ell(\ell+1)}{r^2} + \mu^2 \right). \quad (56)$$

To cast this into a standard Schrödinger-like form, we introduce the tortoise coordinate x , defined by:

$$dx = \frac{dr}{\mathcal{G}(r)}, \quad (57)$$

In this coordinate system, the radial wave equation simplifies to:

$$\left[\frac{d^2}{dx^2} + \omega^2 - \mathcal{U}_{\text{eff}} \right] u_\ell(x) = 0, \quad (58)$$

which describes the propagation of the scalar perturbation in the black hole background, with the potential barrier \mathcal{U}_{eff} . Now, we investigate the boundary behaviors of the eigenfunction by solving the equations as Eq.(58), and the boundary condition at $x \rightarrow \pm\infty$ which are correspond to the physical observers at infinity and near the event horizon, respectively [8]. For $x \rightarrow +\infty$ ($r \rightarrow +\infty$), we have

$$u(x) \simeq e^{i\sqrt{\omega^2 - \mu^2}x}, \quad (59)$$

at the event horizon $r \rightarrow r_+$ ($x \rightarrow -\infty$), we have

$$u(x) \simeq e^{-i\omega x}. \quad (60)$$

The first solution purely outgoing wave corresponds to the requirement that no radiation comes from infinity, while the second solution that means the wave is purely ingoing at the horizon expresses the fact that nothing escapes from the horizon. The effective potentials are shown in Fig.10 . They are positive definite, which guarantees the stability of perturbations, that is, the decaying character of all QNMs.

- Panel (10a) shows the effective potential for different values of the GB coupling parameter α . An increase in the GB coupling α enhances the height of the effective potential barrier, implying a stronger curvature-induced interaction between the scalar field and the modified background geometry.
- Panel (10b) illustrates the influence of the ModMax parameter γ . The effective potential barrier decreases as the ModMax parameter γ increases, indicating that nonlinear electromagnetic effects weaken the confinement of scalar perturbations.
- Panel (10c) presents the effect of varying the scalar field mass μ . As μ increases, the overall potential level rises, reflecting the additional mass contribution to the effective potential. In contrast with the case of a massless field, the potential (potentielQNM) tends to a constant value at spatial infinity, $\lim_{r \rightarrow \infty} \mathcal{U}_{\text{eff}} = \mu^2$, so that the asymptotic behavior of the solutions depends explicitly on the relation between ω and μ .
- Panel (10d) shows the dependence on the multipole number ℓ . Higher values of ℓ increase the centrifugal term, leading to a steeper and higher potential barrier.

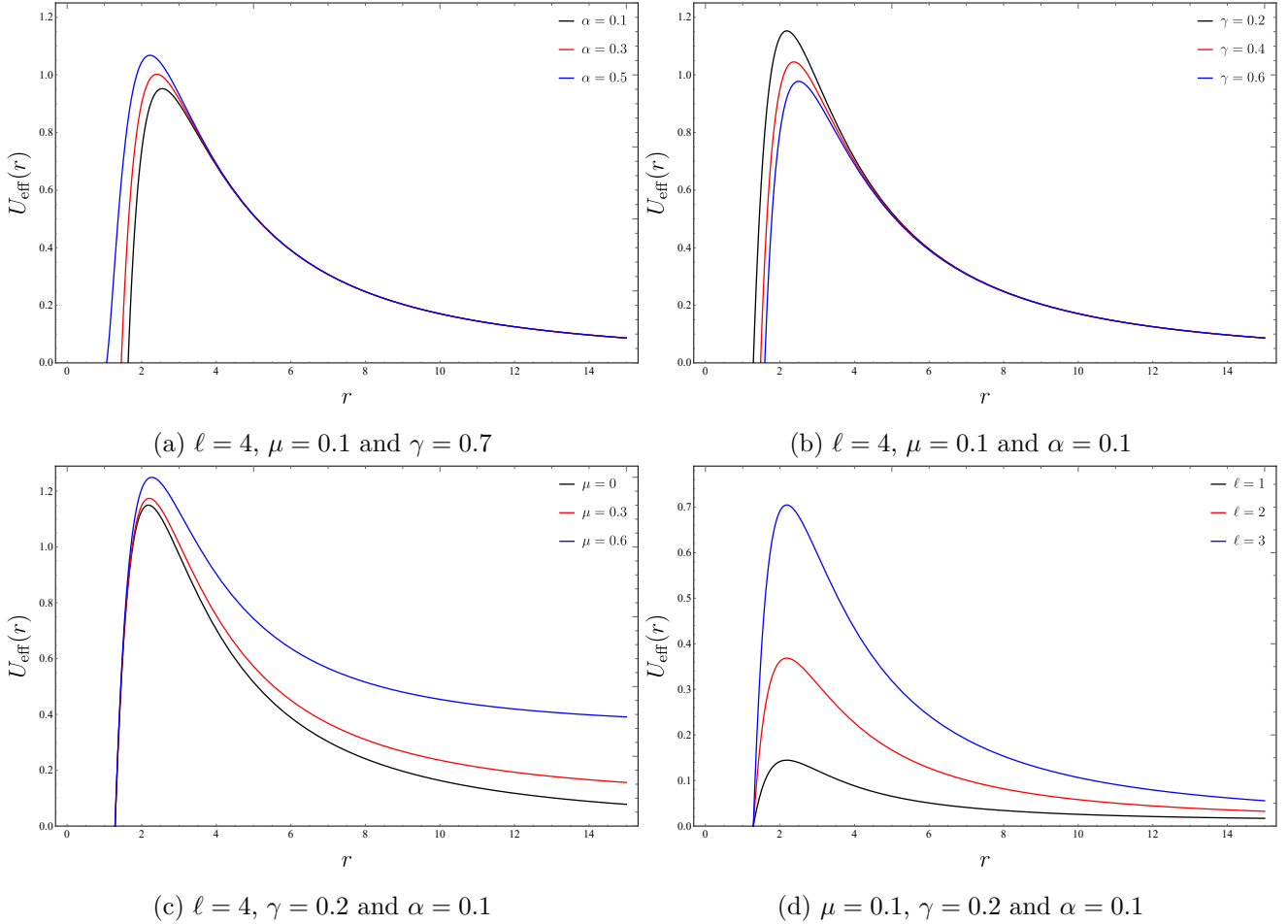


Figure 10: The Variation of the scalar effective potential as a function of radial distance. Parameters: $M = 1, q = 1$.

5.1 WKB method with Padé approximants

The WKB approximation provides an efficient semi-analytical approach for evaluating quasinormal mode frequencies. It is applicable both to black hole scattering problems and to the direct determination of QNMs [64–66]. This method is motivated by the fact that the perturbation equation for a test field resembles the one-dimensional Schrödinger equation with a potential barrier, such as Eq. (58) derived in the previous section. Comprehensive descriptions of the method and the boundary-condition matching procedure can be found in [67], while higher-order extensions are presented in [68–75].

Around the maximum of the effective potential, located at $x = x_0$, the WKB quantization condition governing the complex QNM frequencies takes the generalized form

$$\frac{i(\omega^2 - V_0)}{\sqrt{-2V_0''}} - \sum_{i=2}^N \Lambda_i = n + \frac{1}{2}. \quad (61)$$

In this expression, V_0 and V_0'' denote the value and second derivative of the potential U_{eff} at $x = x_0$, Λ_i are constants arising from higher-order WKB corrections, and $n = 0, 1, 2, \dots$ is the overtone number.

Although the WKB series is asymptotic and does not necessarily converge as the order N increases. In fact, it may begin to diverge beyond a certain order—particularly for small multipole numbers or high overtones. To improve both convergence and accuracy, Padé approximants have been introduced [71]. These are rational functions constructed from the WKB series, and they typically exhibit better

numerical performance and faster convergence compared to the raw polynomial expansion. A Padé approximant of order $N = \hat{m} + \hat{n}$ can be written as

$$P_{\hat{n}/\hat{m}}(\epsilon) = \frac{Q_0 + Q_1\epsilon + \dots + Q_{\hat{n}}\epsilon^{\hat{n}}}{R_0 + R_1\epsilon + \dots + R_{\hat{m}}\epsilon^{\hat{m}}}, \quad (62)$$

where the coefficients $Q_0, Q_1, \dots, Q_{\hat{n}}$ and $R_0, R_1, \dots, R_{\hat{m}}$ are determined by expanding the solution near the top of the potential and matching it through the turning points. In QNM calculations, Padé approximants are commonly applied to the WKB series for ω . Typically, the Padé approximant is applied to the square of the frequency ω^2 , written as:

$$\omega^2 = P_{\hat{n}/\hat{m}}(1). \quad (63)$$

5.2 Numerical results

Due to the complex functional dependencies in Eq. (56), we compute the QNM frequencies by varying these parameters in a systematic manner. Because the WKB approximation is most reliable when the condition $\ell \geq n$ is satisfied[107], our analysis is restricted to scalar field modes obeying this requirement, which correspond to the low-lying quasinormal spectrum. The frequencies are obtained numerically using the sixth-order WKB-Padé approximation applied to the 4D EGB black hole in the presence of ModMax field. By exploring a wide range of multipole numbers ℓ and overtone numbers n , we determine the associated QNM spectrum. The resulting frequencies are presented in Tab.3

summarizes the QNM frequencies of a massive scalar field of a four-dimensional EGB black hole in the presence of ModMax field for the fixed parameters $\gamma = 0.5$, $\alpha = 0.1$, $q = 1$ and $M = 1$, computed using the sixth-order WKB-Padé approximation. For each value of n , the first row is for $\mu = 0$, and the second row is for $\mu = 0.2$. For all modes, the imaginary part of the frequency is negative, confirming that the scalar perturbations are linearly stable in this geometry, in agreement with the positivity of the effective potential outside the event horizon. For a fixed overtone number n , increasing the angular quantum number ℓ increases the real part and makes the imaginary part less negative, resulting in faster oscillations and slower decay. The fundamental modes ($n = 0$) possess the largest quality factors and the longest damping times, particularly at higher ℓ , while higher overtones decay much more rapidly. Overall, Tab.3 highlights the characteristic QNM structure of the 4D ModMax black hole in EGB gravity: low-lying modes are long-lived and oscillatory, whereas higher overtones are short-lived, showing a clear and systematic dependence on both ℓ and n .

ℓ	n	$\omega_R + i\omega_I$	$Q_{Factor} = \frac{\omega_R}{2 \omega_I }$	$t_D = \frac{1}{ \omega_I }$
0	0	0.133509 - 0.101325i	0.65882	9.8692
		0.156357 - 0.0619755i	1.2614	16.135
1	0	0.336845 - 0.0968081i	1.7398	10.330
		0.351836 - 0.0886682i	1.984	11.278
1	1	0.274829 - 0.26096i	0.52657	3.832
		0.290499 - 0.251526i	0.57747	3.9757
2	0	0.555496 - 0.0956137i	2.9049	10.459
		0.565413 - 0.0926064i	3.0528	10.798
1	1	0.517115 - 0.29129i	0.88763	3.433
		0.528174 - 0.282421i	0.93508	3.5408
2	2	0.439941 - 0.421227i	0.52221	2.347
		0.449114 - 0.416959i	0.53856	2.3983
3	0	0.775545 - 0.0952382i	4.0716	10.500
		0.782848 - 0.0937008	4.1774	10.672
1	1	0.754486 - 0.292836i	1.2882	3.4149
		0.761468 - 0.287578	1.3239	3.4773
2	2	0.684053 - 0.468863i	0.72948	2.1328
		0.692904 - 0.46341	0.74761	2.1579
3	3	0.608896 - 0.584008i	0.52131	1.7123
		0.615388 - 0.581213	0.52940	1.7205

Table 3: Quasinormal modes for scalar perturbations calculated using 6th-order WKB-Padé method. Parameters: $\alpha = 0.1$, $\gamma = 0.5$, $q = 1$ and $m = 1$.

We first investigate the impact of the GB coupling parameter α on the quasinormal mode spectrum by analyzing the real and imaginary parts of the frequencies, the quality factor, and the damping time. Fig. 11 displays the variation of these QNM characteristics with $\gamma = 0.5$, $n = 0$, $q = 1$ and $m = 1$.

The upper-left panel shows that the real part of the QNM frequency ω_R increases monotonically with α , indicating that higher-curvature corrections enhance the oscillation frequency of scalar perturbations. The upper-right panel shows that the magnitude of the imaginary part " $|\omega_I|$ " decrease as α increases, implying a reduction in the damping rate and hence a slower decay of the perturbations. Consequently, the quality factor Q_{Factor} displayed in the lower-left panel, increases with α , showing that the oscillations become more persistent when GB effects are stronger. Finally, the damping time t_D shown in the lower-right panel, also increases with α , further confirming that the quasinormal modes become longer-lived for larger coupling strengths. Overall, Fig. 10 demonstrates that the GB coupling significantly modifies both the oscillatory and damping properties of scalar perturbations, leading to faster oscillations and reduced damping as α increases.

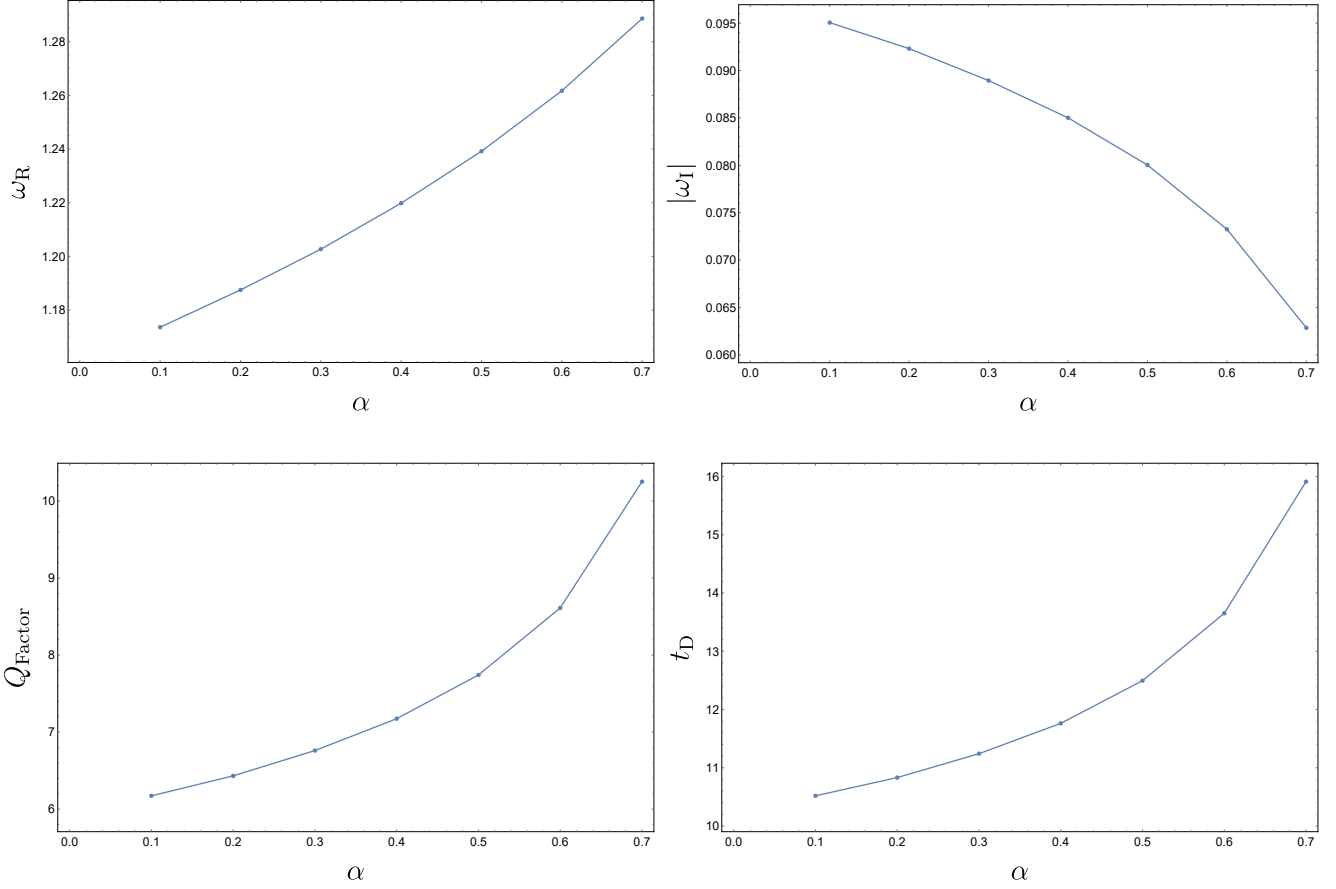


Figure 11: QNM dependence on GB coupling α . Parameters: $\ell = 5$, $M = 1$, $q = 1$, $\gamma = 0.8$ and $\mu = 0.2$.

Next, we compute the quasinormal modes as functions of the ModMax parameter γ for $\ell = 5$, $n = 0$, $\alpha = 0.1$, $q = 1$ and $m = 1$ as shown in Fig. 12. The upper-left panel shows that the real part of the QNM frequency decreases monotonically with increasing γ , indicating that the ModMax nonlinear electromagnetic field reduces the oscillation frequency of scalar perturbations. The upper-right panel displays the behavior of the magnitude of the imaginary part " $|\omega_I|$ ", which increases with increasing α , implying an enhancement of the damping rate, although the trend is not strictly monotonic. As shown in the lower-left panel, the quality factor decreases with increasing γ , indicating that the oscillations become less persistent in the presence of stronger ModMax effects. Finally, the lower-right panel reveals that the damping time decreases as γ increases, confirming that scalar perturbations decay more rapidly for larger values of the ModMax parameter. Overall, Fig. 12 shows that the ModMax parameter suppresses the oscillatory behavior of scalar modes while enhancing their damping, leading to shorter-lived quasinormal oscillations.

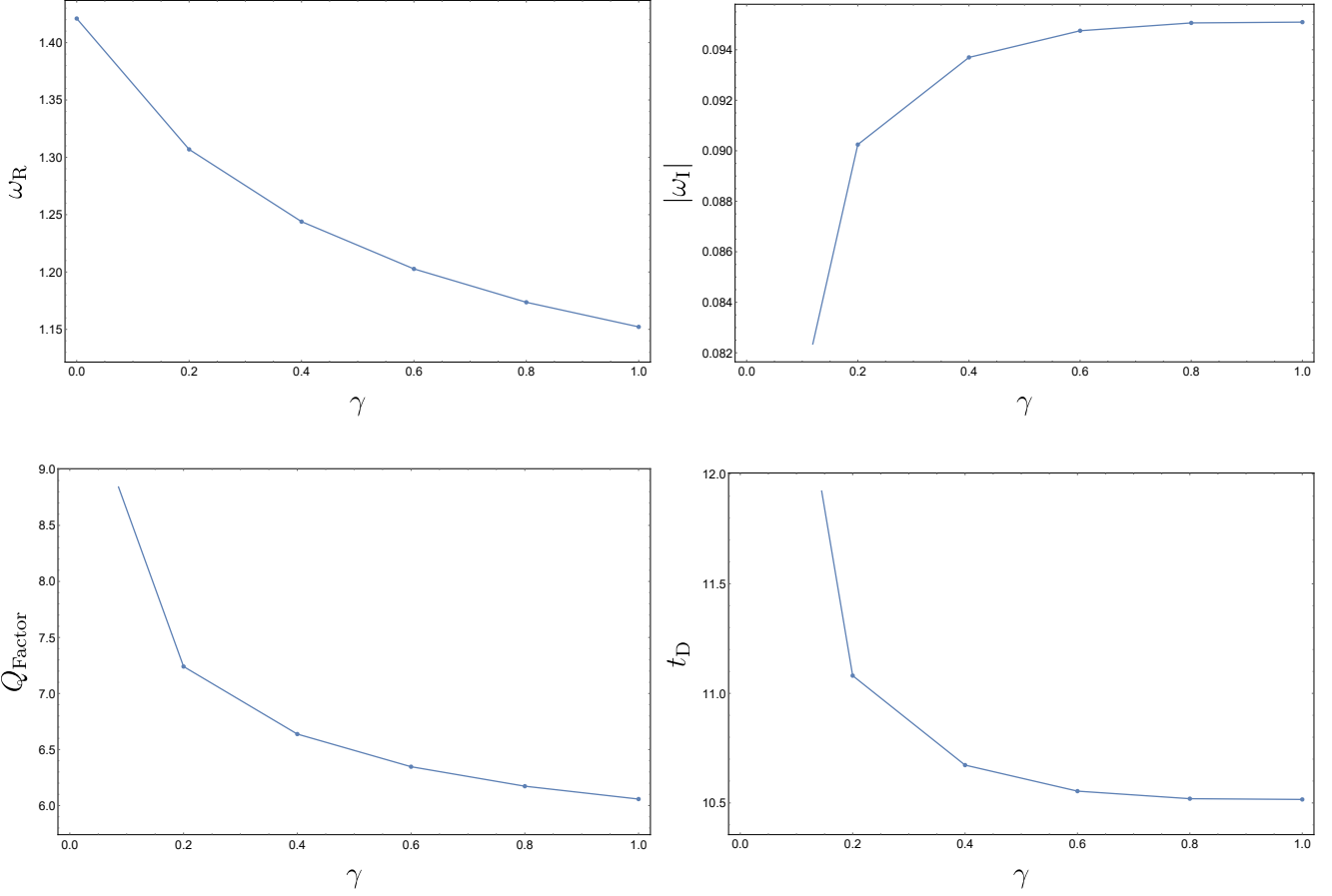


Figure 12: QNM dependence on ModMax Parameter γ . Parameters: $\ell = 5$, $M = 1$, $q = 1$, $\alpha = 0.1$ and $\mu = 0.2$.

As shown in Fig.10c, increasing the field mas μ , causes the peak of the potential to grow. Beyond a certain value, however, the height of this peak becomes lower than the asymptotic value μ^2 . In this situation, no quasinormal modes can exist. If μ is increased further, the peak eventually disappears entirely, and the potential barrier effectively turns into a potential step. It is important to note that quasinormal modes exist only when the maximum of the effective potential, $\mathcal{U}_{\text{eff}}(x = x_0)$, remains larger than μ^2 .

Fig.13 illustrates the influence of the scalar field mass μ on the QNM characteristics for fixed parameters $\gamma = 0.5$, $\alpha = 0.1$, $\ell = 5$, $n = 0$, $q = 1$ and $m = 1$. The upper-left panel shows that the real part of the QNM frequency increases with μ , indicating that heavier scalar fields oscillate at higher frequencies. In contrast, the upper-right panel reveals that the magnitude of the imaginary part $|\omega_I|$ decreases as μ increases, implying a reduction in the damping rate for larger field masses. As a consequence, both the quality factor and the damping time increase with μ , showing that massive scalar perturbations are longer-lived and more oscillatory

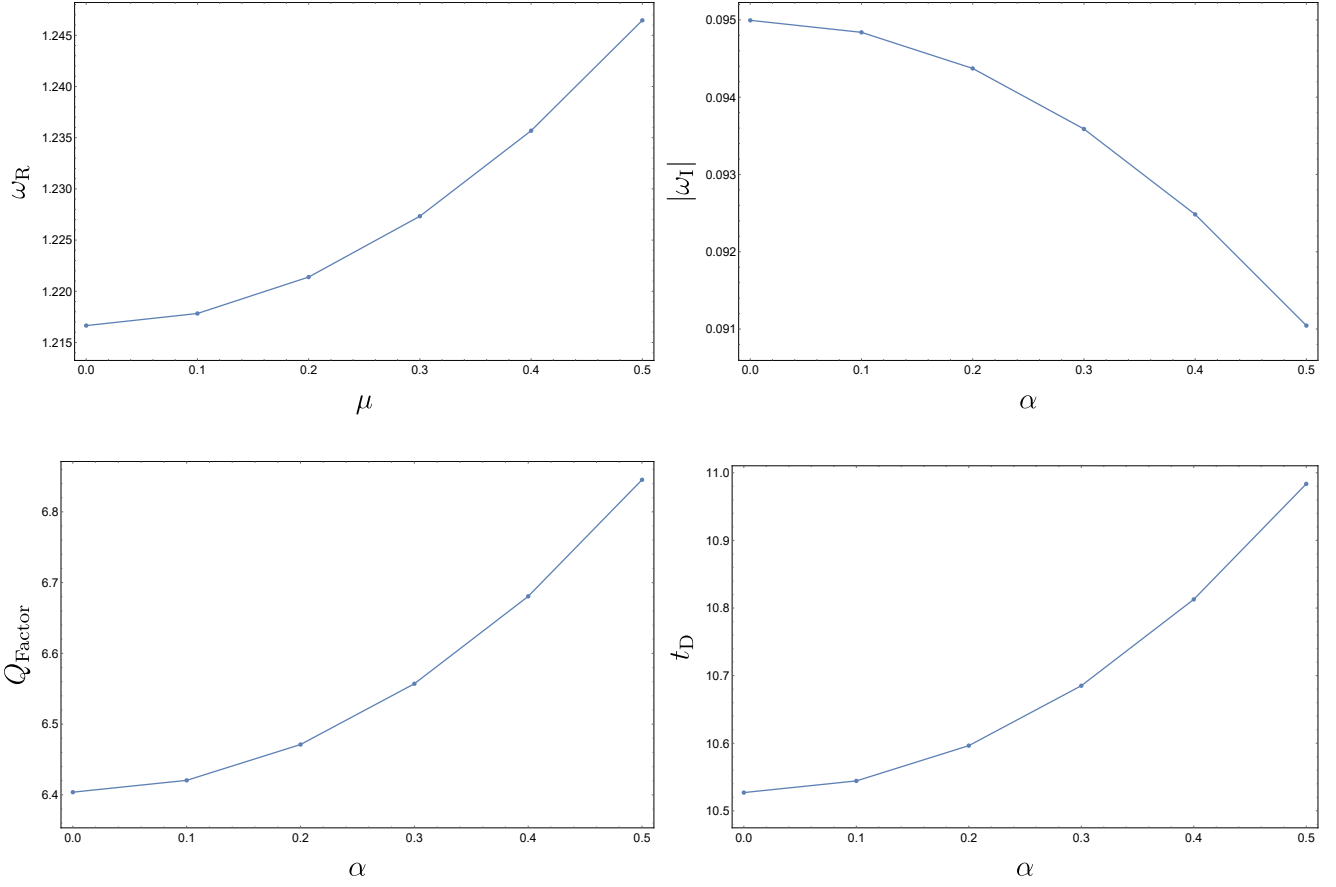


Figure 13: QNM dependence on the scalar field mass μ . Parameters: $\ell = 5$, $M = 1$, $q = 1$, $\alpha = 0.1$ and $\gamma = 0.5$.

5.3 Poschl-Teller method

In the Pöschl-Teller method, the effective potential is approximated by the Pöschl-Teller function [76], which allows Eq. (58) to be solved analytically. In this approach, the effective potential is replaced by

$$\mathcal{U}_{\text{eff}} \simeq \mathcal{U}_{\text{PT}} = \frac{V_0}{\cosh^2[b(x - x_0)]}, \quad (64)$$

where $V_0 = \mathcal{U}_{\text{eff}}(x_0)$ and $b = \sqrt{-\frac{1}{2V_0} \frac{d^2}{dx^2} \mathcal{U}_{\text{eff}}}$. Then, solving Eq. (58) with the Pöschl-Teller approximation leads to the following equation for the calculation of QNMs

$$\omega = ib \left(n + \frac{1}{2} \right) + b \sqrt{\frac{V_0}{\eta^2} - \frac{1}{4}}. \quad (65)$$

This method assumes that both the real and imaginary parts of the frequency depend on the potential and its second derivative evaluated at the maximum. Notably, only the imaginary part, ω_I , is influenced by the overtone number n . Nevertheless, it is not suitable for determining the real part ω_R , except in particular situations such as the eikonal limit $\ell \rightarrow \infty$, or for the fundamental mode $n = 0$. To ensure accuracy in our subsequent analysis, we will keep these limitations in mind and restrict our attention primarily to the eikonal quasinormal modes of the fundamental mode.

Table 4 presents a comparison of the fundamental quasinormal modes for a massless scalar field, calculated using both the Poschl-Teller method and the 6th-order WKB approach. The data clearly

illustrates the characteristic dependence on the multipole number ℓ with the real part of the frequency, increasing significantly due to the stronger centrifugal potential barrier, while the imaginary part, remains remarkably constant, indicating a damping rate independent of ℓ at high values.

γ	ℓ	PT	WKB 6 th order
0.5	5	1.21824 - 0.0951332i	1.21665 - 0.0949939i
	10	2.3216 - 0.0949082i	2.32075 - 0.0948698i
	50	11.1585 - 0.0948259i	11.1584 - 0.0948234i
	100	22.2061 - 0.0948231i	22.206 - 0.0948224i
	500	110.588 - 0.0948222i	110.588 - 0.0948222i
0.8	5	1.1701 - 0.0959234i	1.16847 - 0.0957746i
	10	2.22968 - 0.0956912i	2.22882 - 0.0956502i
	50	10.7164 - 0.0956065i	10.7163 - 0.0956046i
	100	21.3263 - 0.0956036i	21.3262 - 0.0956029i
	500	106.206 - 0.0956027i	106.206 - 0.0956027i

Table 4: QNMs frequencies of the massless scalar field for various values of ℓ . Parameters: $\alpha = 0.1$, $\mu = 0$, $q = 1$, $m = 1$ and $n = 0$.

6 Conclusions

In this work, we performed a detailed study of charged black hole solutions in 4D EGB gravity in the presence ModMax nonlinear electrodynamics. Using the regularization procedure proposed by Glavan and Lin, we derived an exact static and spherically symmetric black hole solution sourced by a purely electric ModMax field, and examine how higher-curvature corrections and nonlinear electromagnetic effects modify the spacetime geometry.

We analyzed the horizon structure and showed that both the GB coupling and the ModMax parameter significantly influence the metric function and the existence of horizons. The thermodynamic properties of the black hole were studied in detail. In particular, the mass-radius relation exhibits a minimum mass, indicating the presence of stable black hole remnants. The Hawking temperature does not diverge as the event horizon shrinks; instead, it has a maximum value, signaling a second-order phase transition, while the heat capacity diverges at the points r_1 and r_2 , which depend on the ModMax parameter and the EGB gravity and reveal regions of local thermodynamic stability. Furthermore, the Helmholtz free energy indicates that large black holes are not globally stable, while small black holes are globally stable configurations.

The motion of massive test particles was investigated using the effective potential approach. We showed that the combined effects of EGB gravity and ModMax electrodynamics lead to notable modifications in particle dynamics. The effective potential has a maximum, which clearly indicates the presence of an unstable circular orbit that depends on the black hole parameters as well as the GB coupling and ModMax electrodynamics. Depending on the energy and angular momentum, particles can follow unstable circular orbits or plunge trajectories that cross the event horizon. We also analyzed the innermost stable circular orbit and found that the existence of the ISCO depends on the parameters α and γ . Increasing the GB coupling decreases the ISCO radius, while increasing the ModMax parameter shifts it outward.

In addition, we studied the effects of EGB gravity and the ModMax field on the quasinormal mode spectrum using a massive scalar field, employing the sixth-order WKB method with Padé approximants and the Pöschl–Teller approximation. The effective potential was shown to be positive outside the horizon, ensuring linear stability. Our results demonstrate that the GB coupling increases the oscillation frequency and reduces the damping rate of scalar perturbations, while the ModMax parameter suppresses

oscillations and enhances damping. The dependence of the quasinormal spectrum on the scalar field mass was also discussed, confirming the absence of unstable modes.

In summary, our analysis highlight the that ModMax nonlinear electrodynamics and GB corrections leave distinct imprints on black hole geometry, thermodynamics, particle motion, and quasinormal spectra. These effects may provide potential observational signatures of nonlinear electrodynamics and higher-curvature gravity in strong-field regimes. Future work could extend this study to rotating solutions, gravitational perturbations, or observational constraints from black hole spectroscopy.

Data Availability Statement

No data were generated or analyzed in this study.

References

- [1] A. Joyce, B. Jain, J. Khouri and Mark Trodden, [Physics Reports](#) **568**,1 (2015)
- [2] L. Barack et al., [Class. Quantum. Grav.](#) **36**, 143001 (2019)
- [3] B. P. Abbott et al., [Phys. Rev. Lett.](#) **116**, 061102 (2016)
- [4] B. P. Abbott et al., [Phys. Rev. Lett.](#) **116**, 241103(2016)
- [5] B. P. Abbott et al., [Phys. Rev. Lett.](#) **118**, 221101 (2017)
- [6] B. P. Abbott et al., [Phys. Rev. Lett.](#) **119**, 141101 (2017)
- [7] D. Lovelock, [J. Math. Phys.](#) **12**, 498 (1971)
- [8] G. Dotti, R. J. Gleiser, [Class. Quantum Grav.](#) **22**, L1 (2005)
- [9] G. Dotti, R. J. Gleiser, [Phys. Rev. D](#) **72**, 044018 (2005)
- [10] R. J. Gleiser, G. Dotti, [Phys. Rev. D](#) **72**, 124002 (2005)
- [11] M. Beroiz, G. Dotti, R. J. Gleiser, [Phys. Rev. D](#) **76**, 024012 (2007)
- [12] R. A. Konoplya, A. Zhidenko, [Phys. Rev. D](#) **77**, 104004 (2008)
- [13] P. Candelas, G. T. Horowitz, A. Strominger, E. Witten, [Nucl. Phys. B](#) **258**, 46 (1985)
- [14] B. Zwiebach, [Phys. Lett. B](#) **156**, 315 (1985)
- [15] B. Zumino, [Physics Reports](#) **137**, 109 (1986)
- [16] D. J. Gross and J. H. Sloan, [Nucl. Phys. B](#) **291**, 41 (1987)
- [17] D. Glavan, C. Lin, [Phys. Lett.B](#) **805**, 135468 (2020)
- [18] Y. Tomozawa, [arXiv:1107.1424](#)
- [19] G. Cognola, R. Myrzakulov, L. Sebastiani, S. Zerbini, [Phys. Rev. D](#) **88**, 024006 (2013)
- [20] Rong-Gen Cai, Li-Ming Cao, N. Ohta, [J. High Energ. Phys.](#) **2010**, 82 (2010)
- [21] H. Lu, Yi Pang, [Phys. Lett. B](#) **809**, 135717 (2020)
- [22] K. Aoki, M. A. Gorji and S. Mukohyama, [Phys. Lett. B](#) **810**, 135843 (2020)

- [23] C. Liu, T. Zhu and Q. Wu, *Chin. Phys. C* **45**, 015105 (2021)
- [24] M. Guo and P. C. Li, *Eur. Phys. J. C* **80**, 588 (2020)
- [25] SW. Wei, YX. Liu, *Eur. Phys. J. Plus* **136**, 436 (2021)
- [26] M. Zubair, M. A. Raza, *Phys. Dark Universe* **40**, 101200 (2023)
- [27] D. Malafarina, B. Toshmatov and N. Dadhich, *Phys. Dark Universe* **30**, 100598 (2020)
- [28] S. A. H. Mansoori, *Phys. Dark Universe* **31**, 100776 (2021)
- [29] X. H. Ge and S. J. Sin, *Eur. Phys. J. C* **80**, 695 (2020)
- [30] J. Rayimbaev, A. Abdujabbarov, B. Turimov and F. Atamurotov, *arXiv:2004.10031*
- [31] S. Chakraborty and N. Dadhich, *Phys. Dark Universe* **30**, 100658 (2020)
- [32] S.D. Odintsov, V.K. Oikonomou, *Phys.Lett B* **805**, 135437 (2020)
- [33] Z. C. Lin, K. Yang, S. W. Wei, Y. Q. Wang and Y. X. Liu, *Eur.Phys. J. C* **80**, 1033 (2020)
- [34] S. Shaymatov, J. Vrba, D. Malafarina, B. Ahmedov and Z. Stuchlik, *Phys. Dark Universe* **30**, 100648 (2020)
- [35] S. Ul Islam, R. Kumar, S. G. Ghosh, *JCAP* **2020**,30 (2020)
- [36] S. G. Ghosh, D. V. Singh, R.Kumar, S. D. Maharaj, *Ann. Phys.* **424**, 168347 (2021)
- [37] J. M. Ladino1, E. Larranaga, *Int. J.Theo. Phys.* **62**, 209 (2023)
- [38] B.Hamil and T. Birkandan, *Nucl. Phys. B* **1020**, 117145 (2025)
- [39] W.Heisenberg, E.Euler, *Z. Physik* **98**, 714 (1936)
- [40] J.Schwinger, *Phys. Rev.* **82**, 664 (1951)
- [41] S.L.Adler, *Ann. Phys.* **67**, 599 (1971)
- [42] V.A.De Lorenci, R.Klippert, M.Novello, J.S. Salim, *Phys. Rev. D* **65**, 063501 (2002)
- [43] Bardeen, J.M., 1968. In: Conference Proceedings of GR5 Non-Singular General Relativistic Gravitational Collapse: Tbilisi, Georgia, USSR, p. 174.
- [44] E. Ayon-Beato, A. Garcia, *Phys. Rev. Lett.* **80**, 5056 (1998)
- [45] M. Born, L. Infeld, *Proc. R. Soc. Lond. A* **144** (852), 425 (1934)
- [46] G.W. Gibbons, D.A. Rasheed, *Nucl. Phys. B* **454**, 185 (1995)
- [47] I. Bandos, K. Lechner, D. Sorokin, P.K. Townsend, *Phys. Rev. D* **102**, 121703 (2020)
- [48] B.P. Kosyakov, *Phys. Lett. B* **810**, 135840 (2020)
- [49] D. Flores-Alfonso, B. A. González-Morales, R. Linares, and M. Maceda, *Phys. Lett. B* **812**, 136011 (2021)
- [50] I. Bandos, K. Lechner, D. Sorokin, P.K. Townsend, *JHEP* **2021**, 22 (2021)
- [51] B. Eslam Panah , N. Heidari, *J.High Energy Astrophysics* **45**, 181 (2025)

[52] B. Eslam Panah, *Phys. Lett. B* **868**, 139711 (2025)

[53] B. Eslam Panah, B Hazarika, P Phukon, *PTEP* **2024**, 083 (2024)

[54] A. Q. Baptista and M. L. Penafiel, *Phys. Rev D* **112**, 024037 (2025)

[55] R. C. Pantig, L. Mastrototaro, G. Lambiase, and A. Övgün, *Eur.Phys. J. C* **82**, 1155 (2022).

[56] J. Barrientos, A. Cisterna, D. Kubiznak, and J. Oliva, *Phys. Lett. B* **834**, 137447 (2022)

[57] S. Habib Mazharimousavi, *Int. J.Geo. Meth.Mod. Phys.* **19**, 2250204 (2022)

[58] E. Guzman-Herrera and N. Breton, *J. Cosmol. Astropart.Phys.* **01**, 041 (2024)

[59] E. Guzman-Herrera, A. Montiel, and N. Breton, *J. Cosmol.Astropart. Phys.* **11**, 002 (2024)

[60] A. Bokulic and C. A. Herdeiro, *Phys. Rev. D* **111**, 064046 (2025)

[61] B. Eslam Panah, B. Hamil, Manuel E. Rodrigues, [arXiv:2512.22654 \[gr-qc\]](https://arxiv.org/abs/2512.22654)

[62] C. Lanczos, *Ann. of Math.* **39**, 842 (1938).

[63] J.T. Wheeler, *Nucl. Phys.B* **268**, 737 (1986)

[64] C.V. Vishveshwara, *Nature* **227**, 936 (1970)

[65] K.D. Kokkotas, B.G. Schmidt, *Living Rev. Relativ.* **2**, 2 (1999).

[66] S. S. Hegde, V. Subramanyan, B. Bradlyn, and S. Vishveshwara, *Phys. Rev. Lett.* **123**, 156802 (2019)

[67] R. A. Konoplya, *Rev. Mod. Phys.* **83**, 793 (2011)

[68] S. Iyer and C. M. Will, *Phys. Rev. D* **35**, 3621 (1987)

[69] R. A. Konoplya, *Phys. Rev. D* **68**, 024018 (2003)

[70] R. A. Konoplya, *J. Phys. Stud.* **8**, 93 (2004)

[71] J. Matyjasek and M. Opala, *Phys. Rev. D* **96**, 024011 (2017)

[72] B. Hamil, B. C. Lutfuoglu, *Fortsch. Phys.* **73**, 2400105 (2025)

[73] B. Hamil, B. C. Lutfuoglu, *Ann. Phys.* **472**, 169861 (2025)

[74] B. Hamil, B. C. Lutfuoglu, *Dark Universe* **44**, 101484 (2024)

[75] B. Hamil, B. C. Lutfuoglu, *Gen Relativ Gravit* **57**, 140 (2025)

[76] V. Ferrari, B. Mashhoon, *Phys. Rev. D* **30**, 295 (1984)